New Cost-Effective Halide Solid Electrolytes for All-Solid-State Batteries: Mechanochemically Prepared Fe^{3+}-Substituted Li_2ZrCl_6

Hiram Kwak, Daseul Han, Jeyne Lyoo, Juhyoun Park, Sung Hoo Jung, Yoonjae Han, Gihan Kwon, Hansu Kim, Seung-Tae Hong, Kyung-Wan Nam,* and Yoon Seok Jung*

Owing to the combined advantages of sulfide and oxide solid electrolytes (SEs), that is, mechanical sinterability and excellent (electro)chemical stability, recently emerging halide SEs such as Li_3YCl_6 are considered to be a game changer for the development of all-solid-state batteries. However, the use of expensive central metals hinders their practical applicability. Herein, a new halide superionic conductors are reported that are free of rare-earth metals: hexagonal close-packed (hcp) Li_2ZrCl_6 and Fe^{3+}-substituted Li_2ZrCl_6, derived via a mechanochemical method. Conventional heat treatment yields cubic close-packed monoclinic Li_2ZrCl_6 with a low Li^+ conductivity of 5.7×10^{-6} S cm^{-1} at 30 °C. In contrast, hcp Li_2ZrCl_6 with a high Li^+ conductivity of 4.0×10^{-4} S cm^{-1} is derived via ball-milling. More importantly, the aliovalent substitution of Li_2ZrCl_6 with Fe^{3+}, which is probed by complementary analyses using X-ray diffraction, pair distribution function, X-ray absorption spectroscopy, and Raman spectroscopy measurements, drastically enhances the Li^+ conductivity up to ≈ 1 mS cm^{-1} for $Li_{2.25}Zr_{0.75}Fe_{0.25}Cl_6$. The superior interfacial stability when using $Li_{2+x}Zr_{1-x}Fe_xCl_6$, as compared to that when using conventional Li_6PS_5Cl, is proved. Furthermore, an excellent electrochemical performance of the all-solid-state batteries is achieved via the combination of Li_2ZrCl_6 and single-crystalline $LiNi_{0.88}Co_{0.11}Al_{0.01}O_2$.

For the development of next-generation all-solid-state Li batteries offering ultimate safety and high performance, solid electrolytes (SEs) with a high Li^+ conductivity of at least 10^{-3} S cm^{-1} at room temperature are a prerequisite.[1–8] This can be satisfied by different types of inorganic compounds such as sulfides (e.g., $Li_{6-x}PS_{5-y}X_{1+y}$ [X = Cl, Br; y = 0.0–0.5], 1–10 mS cm^{-1}),[9] oxides (e.g., $Li_7La_3Zr_2O_{12}$, 0.1–1 mS cm^{-1}),[10] borohydrides

(e.g., $0.7Li(CB_9H_{10})-0.3Li(CB_{11}H_{12})$, 6.7 mS cm^{-1}),[11,12] and halides (e.g., Li_3YX_6 [X = Cl, Br], 0.51–1.7 mS cm^{-1}).[13,14] Thus far, oxide and sulfide SEs have been the most commonly investigated candidates. However, their pros and cons counteract each other. Oxide SEs possess high intrinsic electrochemical oxidation stabilities and relatively acceptable chemical stabilities; however, owing to their brittle nature, it is difficult to integrate them in devices.[3,10,15–17] On the other hand, the most important advantage of sulfide SEs, that is, mechanical deformability, which enables scalable cold-pressing-based fabrication protocols, is offset by their poor (electro)chemical stabilities.[3,16,18–20] On exposing sulfide SEs to humid air, the evolution of toxic H_2S gases occurs.[21–26] Moreover, sulfide SEs exhibit oxidative decomposition at <3 V (vs Li/Li$^+$) and are also incompatible with conventional layered $LiMO_2$ (M = Ni, Co, Mn, and Al) cathodes.[16,19,27] This issue can be alleviated by using protective coatings, such as $LiNbO_3$ and $Li_{3-x}B_{1-x}C_xO_3$;[7,27] however, this constitutes additional processing costs. Furthermore, the oxidative decomposition of sulfide SEs at the surface of conductive carbon additives is unavoidable.[28–31]

Recently, through reinvestigations on halide SEs, several compounds exhibiting Li^+ conductivities exceeding 10^{-4} S cm^{-1} have been identified.[13,32–36] Asano and coworkers reported that trigonal Li_3YCl_6 and monoclinic Li_3YBr_6 showed high Li^+

H. Kwak, J. Park, Dr. S. H. Jung, Y. Han, Prof. Y. S. Jung
Department of Chemical and Biomolecular Engineering
Yonsei University
Seoul 03722, South Korea
E-mail: yoonsjung@yonsei.ac.kr
H. Kwak, J. Park, Y. Han, Prof. H. Kim
Department of Energy Engineering
Hanyang University
Seoul 04763, South Korea

The ORCID identification number(s) for the author(s) of this article can be found under https://doi.org/10.1002/aenm.202003190.

D. Han, Prof. K.-W. Nam
Department of Energy and Materials Engineering
Dongguk University
Seoul 04620, South Korea
E-mail: knam@dongguk.edu
J. Lyoo, Prof. S.-T. Hong
Department of Energy Science and Engineering
DGIST (Daegu Gyeongbuk Institute of Science and Technology)
Daegu 42988, South Korea
Dr. G. Kwon
National Synchrotron Light Source II
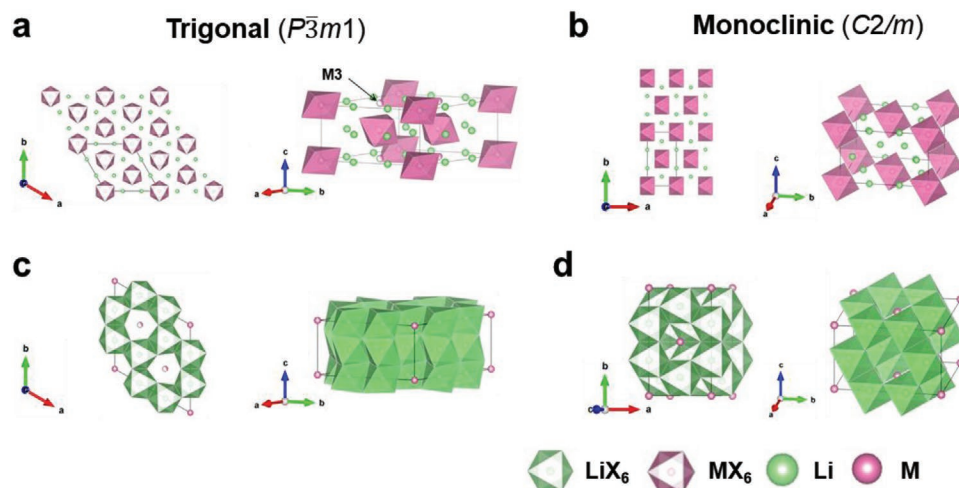Brookhaven National Laboratory
Upton, NY 11973, USA

**ADVANCED
SCIENCE NEWS**
www.advancedsciencenews.com

**ADVANCED
ENERGY
MATERIALS**
www.advenergymat.de

Figure 1. Crystal structures outlined with the unit cells for a) trigonal and b) monoclinic Li_3MCl_6 (or Li_2MCl_6). c,d) Corresponding Li^+ migration pathways.

conductivities of 0.51 and 1.7 mS cm^{-1}, respectively.[13] These high Li$^+$ conductivities are nested in the weak bond strength between the monovalent halide anion and Li$^+$.[13,32] More importantly, halide SEs, especially chloride compounds, exhibit the combined advantages of sulfide and oxide SEs: deformability and excellent (electro)chemical stability.[13,16,32,37] Pellet-type all-solid-state cells employing halide SEs can be fabricated by compacting powders at room temperature, similar to those using sulfide SEs.[13,33] Moreover, uncoated LiCoO$_2$ coupled with halide SEs showed high capacities and high initial Coulombic efficiencies, comparable to those obtained using conventional liquid electrolyte cells.[13,33]

The halide SEs that have been identified thus far can be classified into three categories:[32] i) those with group 3 elements (Sc, Y, and La-Lu), ii) those with group 13 elements (Al, Ga, and In), and iii) those with divalent metals (e.g., first transition metals). Among these, several compounds under the first two categories showed acceptable Li$^+$ conductivities exceeding 10^{-4} S cm^{-1}; their corresponding main (or representative) crystal structures are displayed in **Figure 1** and Figure S1, Supporting Information. The trigonal (space group $P\bar{3}m1$, Figure 1a) or orthorhombic structures (space group $Pnma$ for phase I and phase II,[35] Figure S1, Supporting Information) have hexagonal close-packed (hcp) anionic structures, whereas the monoclinic structure (space group $C2/m$, Figure 1c), has a cubic close-packed (ccp) anionic structure. In compounds based on trivalent metal ions (e.g., Li$_3$YCl$_6$), overall, the octahedral sites are occupied by Li$^+$, M^{3+}, and vacancies in a ratio of 3:1:2.[32] It is noted that the successful identification of highly Li$^+$-conductive halide SE compounds was achieved using a mechanochemical method. The Li$^+$ conductivity of trigonal Li$_3$YCl$_6$, an isostructure of Li$_3$ErCl$_6$, was high (0.51 mS cm^{-1}) only in the ball-milled (BM) sample.[13,34] Annealing at an elevated temperature of 550 °C resulted in a significant reduction in Li$^+$ conductivity to 3 × 10^{-5} S cm^{-1}, despite a lack of change in the structural framework. Zeier and coworkers conducted pair distribution function (PDF) analyses and showed that the M2/M3 (M = Y or Er) site disordering, caused by the mechanochemical synthesis process, was responsible for the large difference in Li$^+$ conductivity

(Figure 1a).[34] Furthermore, Sun and coworkers achieved high Li$^+$ conductivities of 1.49 mS cm^{-1} at 25 °C for monoclinic Li$_3$InCl$_6$ using mechanochemical milling and subsequent annealing at 260 °C;[33] in contrast, samples prepared by conventional solid-state synthesis exhibited low Li$^+$ conductivities of ≈10^{-5} S cm^{-1}.[38] Recently, Sc-based halide SEs—monoclinic Li$_x$ScCl$_{3+x}$ (maximum = 3 mS cm^{-1}) and disordered-spinel Li$_2$Sc$_{2/3}$Cl$_4$ (1.5 mS cm^{-1})—were also reported.[36,39]

Despite these advances in halide SEs, high Li$^+$ conductivities reaching ≈10^{-3} S cm^{-1} have only been achieved using scarce and expensive elements such as Y, Er, Sc, and In; in most cases, rare-earth metals were used.[13,32–36] Moreover, the use of tetravalent metals has remained scarce. Nazar and coworkers identified new orthorhombic phases (Figure S1, Supporting Information) via the aliovalent substitution of M^{3+} in Li$_3$MCl$_6$ (M = Er, Y) with Zr^{4+}.[35] However, a high Li$^+$ conductivity of ≈10^{-3} S cm^{-1} was obtained for partial substitution (x = 0.30–0.35 in Li$_{3-x}$Er$_{1-x}$Zr$_x$Cl$_6$, x = 0.2–0.5 in Li$_{3-x}$Y$_{1-x}$Zr$_x$Cl$_6$), and results for the fully substituted composition of Li$_2$ZrCl$_6$ were not presented.

Inspired by these previous studies, we herein report on new halide SEs free of rare-earth metals and prepared via a mechanochemical process: Li$_2$ZrCl$_6$ and Fe^{3+}-substituted Li$_2$ZrCl$_6$. Zr is considerably more abundant in nature, approximately by an order of magnitude compared with Y or Sc and by more than three orders of magnitude compared with In.[40] Li$_2$ZrCl$_6$, prepared via heat treatment or ball-milling, exhibits drastic differences in terms of both crystal structure (ccp vs hcp) and Li$^+$ conductivity (5.7 × 10^{-6} vs 4.0 × 10^{-4} S cm^{-1} at 30 °C). More importantly, Fe^{3+}-substituted Li$_2$ZrCl$_6$ shows a maximum conductivity of 0.98 mS cm^{-1} (Li$_{2.25}$Zr$_{0.75}$Fe$_{0.25}$Cl$_6$) with the lowest activation energy of 0.346 eV. Complementary analyses using X-ray diffraction (XRD), PDF, X-ray absorption spectroscopy (XAS), and Raman spectroscopy measurements are employed to probe the low-crystalline structure of the samples. Furthermore, the excellent compatibility of Li$_2$ZrCl$_6$ and/or Fe^{3+}-substituted Li$_2$ZrCl$_6$ with LiCoO$_2$ or single-crystalline LiNi$_{0.88}$Co$_{0.11}$Al$_{0.01}$O$_2$ (single-NCA88) is demonstrated by the high electrochemical performance and ex situ X-ray photoelectron spectroscopy (XPS) results.
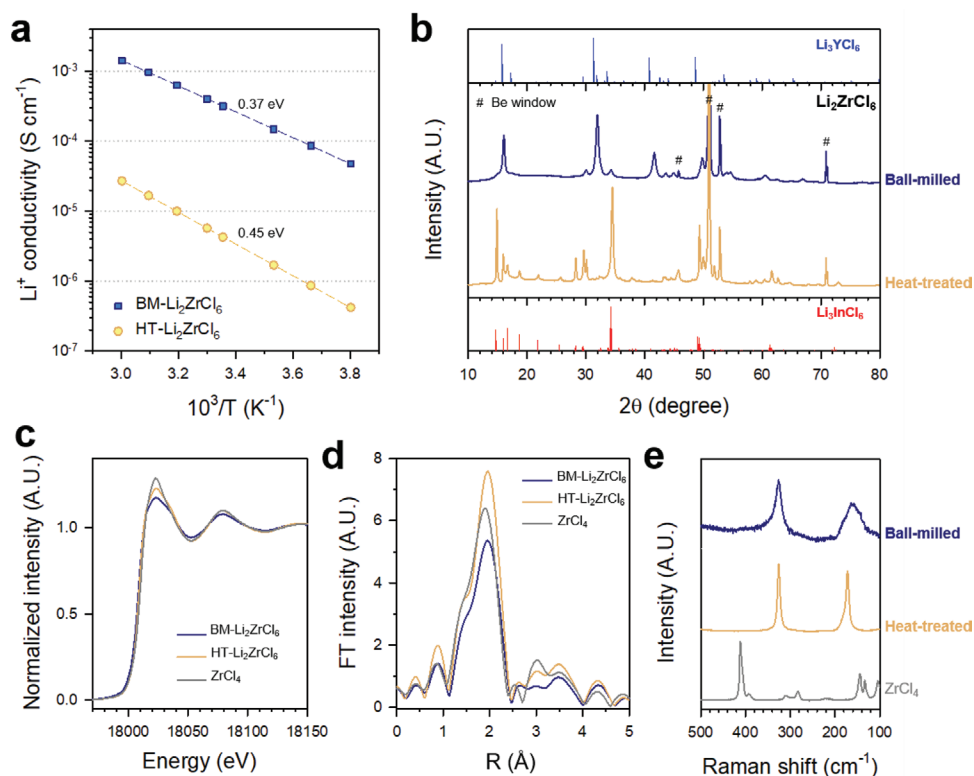
ADVANCED
SCIENCE NEWS

www.advancedsciencenews.com

ADVANCED
ENERGY
MATERIALS

www.advenergymat.de

Figure 2. Characterization of ball-milled (BM) and heat-treated (HT) Li_2ZrCl_6. a) Arrhenius plots of Li^+ conductivities, b) XRD patterns, c) Zr K-edge XANES spectra, d) Zr K-edge EXAFS spectra, and e) Raman spectra for BM- and HT-Li_2ZrCl_6. Bragg peaks for Li_3YCl_6[13] and Li_3InCl_6[32] are also shown at the top and bottom, respectively, in (b). Raman spectrum for $ZrCl_4$ is also compared in (e).

Two Li_2ZrCl_6 powder samples were prepared by ball-milling a stoichiometric mixture of $LiCl$ and $ZrCl_4$ with or without the subsequent heat treatment at 260 °C; these were denoted as heat-treated (HT)-Li_2ZrCl_6 and BM-Li_2ZrCl_6, respectively. The excellent deformability of BM-Li_2ZrCl_6 was confirmed by the flattened surface of the pellets prepared by cold-pressing SE powders at 370 MPa (Figure S2, Supporting Information). Moreover, the Li^+ conductivity and porosity of the pellets as a function of applied pressure for BM-Li_2ZrCl_6, shown in Figure S3, Supporting Information, indicate that the applied pressure of 370 MPa is high enough for densification and saturation in Li^+ conductivity. The Li^+ conductivities of the cold-pressed pellets of BM- and HT-Li_2ZrCl_6 were measured using the AC impedance method with Li^+-blocking Ti/SE/Ti symmetric cells fabricated at an applied pressure of 370 MPa. The corresponding Nyquist plots at 30 °C are shown in Figure S4, Supporting Information. As the electronic conductivity of BM-Li_2ZrCl_6, as determined via chronoamperometry measurements (Figure S5, Supporting Information), was sufficiently low (5.8×10^{-10} S cm^{-1}), its contribution toward the overall electrical conductivity obtained by the AC impedance data could be neglected. Arrhenius plots of the resulting Li^+ conductivities with a wide temperature range from −10 to 60 °C are displayed in **Figure 2**a. BM-Li_2ZrCl_6 showed a Li^+ conductivity of 4.0×10^{-4} S cm^{-1} at 30 °C with an activation energy of 0.37 eV. In contrast, for the HT sample, a considerably lower Li^+ conductivity of 5.7×10^{-6} S cm^{-1} and a higher activation energy of 0.45 eV were obtained.

The XRD patterns of HT- and BM-Li_2ZrCl_6 are shown in Figure 2b. The XRD signal of HT-Li_2ZrCl_6 matched that of

the ccp monoclinic Li_3InCl_6 (space group $C2/m$) shown in Figure 1b,d.[33] The results of Rietveld refinement are also provided in Figure S6 and Table S1, Supporting Information. For halide SEs, the ccp monoclinic lattice structure was observed in the compounds, where a large difference between the ionic radii of the central metal cation and the halide anion exists. These include Li_3MBr_6,[41] Li_3MI_6,[42] and Li_3ScCl_6.[36] Considering the significantly smaller ionic radius of Zr^{4+} (72 pm), as compared with other metal ions used to form the hcp structure, such as Y^{3+} (90 pm), Tb^{3+} (92.3 pm), and Lu^{3+}(86.1 pm), the evolution of monoclinic Li_2ZrCl_6 for the HT sample could be understood. Despite being an isostructure of highly conductive Li_3InCl_6 (1.49 mS cm^{-1}) and Li_3ScCl_6 (≈3 mS cm^{-1}), the considerably lower Li^+ conductivity of HT-Li_2ZrCl_6 (5.7×10^{-6} S cm^{-1}) is intriguing. To explain this, several factors could be considered: i) insufficient amount of mobile charge carriers of Li^+, ii) strong Coulombic repulsion between Zr^{4+} and Li^+, which may lead to a higher activation barrier for Li^+ transport, and iii) reduced volume of Li^+ channels.[26,43] It should be noted that HT-Li_2ZrCl_6 exhibited a smaller lattice volume (417.458 Å^3) than both Li_3InCl_6 (426.409 Å^3) and Li_3ScCl_6 (420.730 Å^3).[32,36] Specifically, based on the XRD data for Li_3InCl_6, while HT-Li_2ZrCl_6 showed a marginal peak shift at ≈16.0° and ≈16.7° corresponding to the (020) and (110) planes, a noticeable peak shift occurred at ≈15° corresponding mainly to the (001) plane; this indicates asymmetric shrinkage of the lattice volume along the c axis (Figure S7, Supporting Information).

BM-Li_2ZrCl_6 exhibited broad main peaks in its XRD signal, which is common for mechanochemically prepared samples

and indicates low crystallinity and/or structural disorder (Figure 2b).[13,33,34] Unexpectedly, the main peaks for BM-Li_2ZrCl_6 matched those of hcp trigonal Li_3YCl_6 (space group $P\overline{3}m1$, Figure 1a,d).[13] The different structures of Li_2ZrCl_6, depending on the preparation protocols, are in stark contrast to that of Li_3YCl_6, for which heat treatment did not alter the trigonal anionic framework.[13] As stated earlier, considering the significantly smaller radius of Zr^{4+} (72 pm) than that of Y^{3+} (90 pm), the appearance of an hcp structure in the BM sample is abnormal; this implies that the hcp structure for Li_2ZrCl_6 is metastable, which is in-line with the annealing test results (Figure S8, Supporting Information). Annealing at 260 °C for several minutes resulted in a phase transition from hcp to ccp (monoclinic) and a corresponding rapid decrease in Li^+ conductivity. Computational calculations regarding the structural stability of Li_2ZrCl_6 are expected to be an interesting topic.[34,44,45] Compared with the Bragg peaks for Li_3YCl_6, the positive shift in the peaks for Li_2ZrCl_6 reflects the smaller lattice size of Li_2ZrCl_6, which is due to the smaller ionic radius of Zr^{4+} (72 pm) compared to that of Y^{3+} (90 pm). This is also confirmed by the characterization of a series of $Li_{3-x}Y_{1-x}Zr_xCl_6$ using XRD, Li^+ conductivity, and XAS measurements (Figures S9 and S10, Supporting Information). As the amount of substituted Zr^{4+} increased, the XRD peaks gradually shifted in the positive direction (Figure S9a, Supporting Information). In a previous study on high-crystalline $Li_{3-x}Y_{1-x}Zr_xCl_6$ ($0 \leq x \leq 0.8$) prepared via the conventional high-temperature heat treatment, rigorous structural analyses using single-crystal XRD measurements enabled the identification of new orthorhombic phases (phase II at $\approx 0.15 \leq x \leq 0.27$, phase III at $x \geq 0.35$) whose Bragg positions significantly overlapped those of the trigonal phase; their crystal structures are shown in Figures 1a,c, and Figure S1, Supporting Information. In this regard, the possibility of an orthorhombic structure of BM-Li_2ZrCl_6 cannot be ruled out completely.[35] However, the broad peaks of BM-Li_2ZrCl_6 make it difficult to determine whether the phase is trigonal or orthorhombic, which are common in the hcp-based structure.

Several reports showed that the site disordering existing in the trigonal structured halide Li_3MCl_6 (M = Y, Er, space group: $P\overline{3}m1$) SEs could increase ionic conductivity.[13,46] To verify the existence of this site disordering in BM-Li_2ZrCl_6, preliminary PDF analysis was performed and shown in Figure S11, Supporting Information. Comparison with theoretically generated PDFs $G(r)$ with varying degrees of M2-M3 site disordering demonstrates the existence of M2-M3 site disordering in BM-Li_2ZrCl_6, which could be beneficial for ionic transport. Further quantitative structural analysis including neutron PDFs will follow to pinpoint the atomic position of Li and resolve the detailed structure of BM-Li_2ZrCl_6.

In order to probe the local environment around the Zr atoms in BM- and HT-Li_2ZrCl_6, Zr K-edge XAS analyses were conducted. Figure 2c shows the normalized Zr K-edge X-ray absorption near-edge structure (XANES) spectra for BM- and HT-Li_2ZrCl_6. The identical main edge position at around 18 020 eV for both the samples and the reference $ZrCl_4$ confirms the tetravalent oxidation state of Zr.[47,48] Furthermore, extended X-ray absorption fine structure (EXAFS) spectra for BM-, HT-Li_2ZrCl_6, and $ZrCl_4$ (Figure 2d) show the identical first peak at a distance of ≈ 2 Å for the shortest Zr—Cl coordi-

nation, revealing the octahedral coordination of Zr ($ZrCl_6^{2-}$) in both samples.[49] The lower first peak intensity of BM-Li_2ZrCl_6 than that of HT-Li_2ZrCl_6 suggests a considerably reduced crystallinity during the mechanochemical process. Further structural information regarding the $ZrCl_6^{2-}$ octahedra was acquired by Raman spectroscopy measurements (Figure 2e). The broad peaks for the BM sample reflects the disordered structure.[50,51] The Raman spectrum of $ZrCl_4$ showed characteristic signatures of zigzag, polymer-like chain-structured $[(ZrCl_{4/2})Cl_2]_n$ of bridged octahedra; a detailed description is provided in Figure S12, Supporting Information.[52] In contrast, for both BM- and HT-Li_2ZrCl_6, the signatures of bridging octahedra disappeared and two strong peaks at ≈ 325 and ≈ 161 cm^{-1} appeared. These peaks are assigned as the A_{1g} stretching and the F_{2g} bending, which were generally observed for a series of elpasolite compounds ($A_2^+B^+M^{3+}X^-_6$: Cs_2LiYCl_6, Cs_2NaYCl_6, and Cs_2NaYBr_6).[53,54]

The aliovalent substitution of Zr^{4+} in Li_2ZrCl_6 with a trivalent metal Fe^{3+} was attempted. A series of Fe^{3+}-substituted Li_2ZrCl_6 samples, $Li_{2+x}Zr_{1-x}Fe_xCl_6$, were prepared by ball-milling a stoichiometric mixture of LiCl, $ZrCl_4$, and $FeCl_3$. **Figures 3**a and 3b show the XRD patterns of nominal composition, $Li_{2+x}Zr_{1-x}Fe_xCl_6$, over a wide range of x values ($0 \leq x \leq 0.5$) and the corresponding Li^+ conductivities with activation energies, respectively. Arrhenius plots of Li^+ conductivity are shown in Figure S13, Supporting Information. As shown in the XRD patterns (Figure 3a), as the amount of Fe increased up to $x = \approx 0.25$, a slight positive shift in the peak position was observed without a noticeable evolution of new peaks, which implies the formation of the solid-solution phase. A slight positive shift in the peaks upon Fe^{3+}-substitution is likely due to the smaller ionic radius of Fe^{3+} (64.5 pm) than that of Zr^{4+} (72 pm). In contrast, the composition at $x \geq 0.30$ showed strong peaks at $\approx 30°$ and $\approx 32°$, which correspond to an impurity of LiCl (ICSD No. 65485). Thus, the solubility limit of Fe^{3+} for BM-Li_2ZrCl_6 is determined to be $x = 0.25-0.30$. This is supported by the Li^+ conductivity results at 30 °C (Figure 3b). Li^+ conductivities, as a function of x in $Li_{2+x}Zr_{1-x}Fe_xCl_6$, exhibited a volcano-shape curve which is opposite to the shape of the corresponding activation energy curve. The increase in Li^+ conductivity (or decrease in activation energy) of $Li_{2+x}Zr_{1-x}Fe_xCl_6$ from $x = 0.00$ to $x = 0.25$ could be interpreted as the positive effect of the aliovalent substitution of Fe^{3+} in the lattice.[26,44,55–57] In contrast, the subsequent decrease in Li^+ conductivity (or increase in activation energy) is caused by the segregation of insulating LiCl. Specifically, the maximum Li^+ conductivity reached 0.98 mS cm^{-1} with the lowest activation energy of 0.346 eV for $x = 0.25$. It is noteworthy that a Li^+ conductivity of 1 mS cm^{-1} was achieved using cost-effective Zr and Fe metals, instead of the conventional use of rare-earth metals; to the best of the authors' knowledge, such an approach for the synthesis of halide SEs has not been reported thus far. Furthermore, aliovalent substitutions for Li_2ZrCl_6 with alternative trivalent metal ions of Cr^{3+} (61.5 pm) or V^{3+} (64 pm) proved effective for enhancing Li^+ conductivity (Figure 3b). As observed for Fe^{3+}-substituted Li_2ZrCl_6, a marginal change in the XRD pattern for V^{3+}-substituted Li_2ZrCl_6 was confirmed (Figure S14, Supporting Information), which is also indicative of the formation of the solid-solution phase.

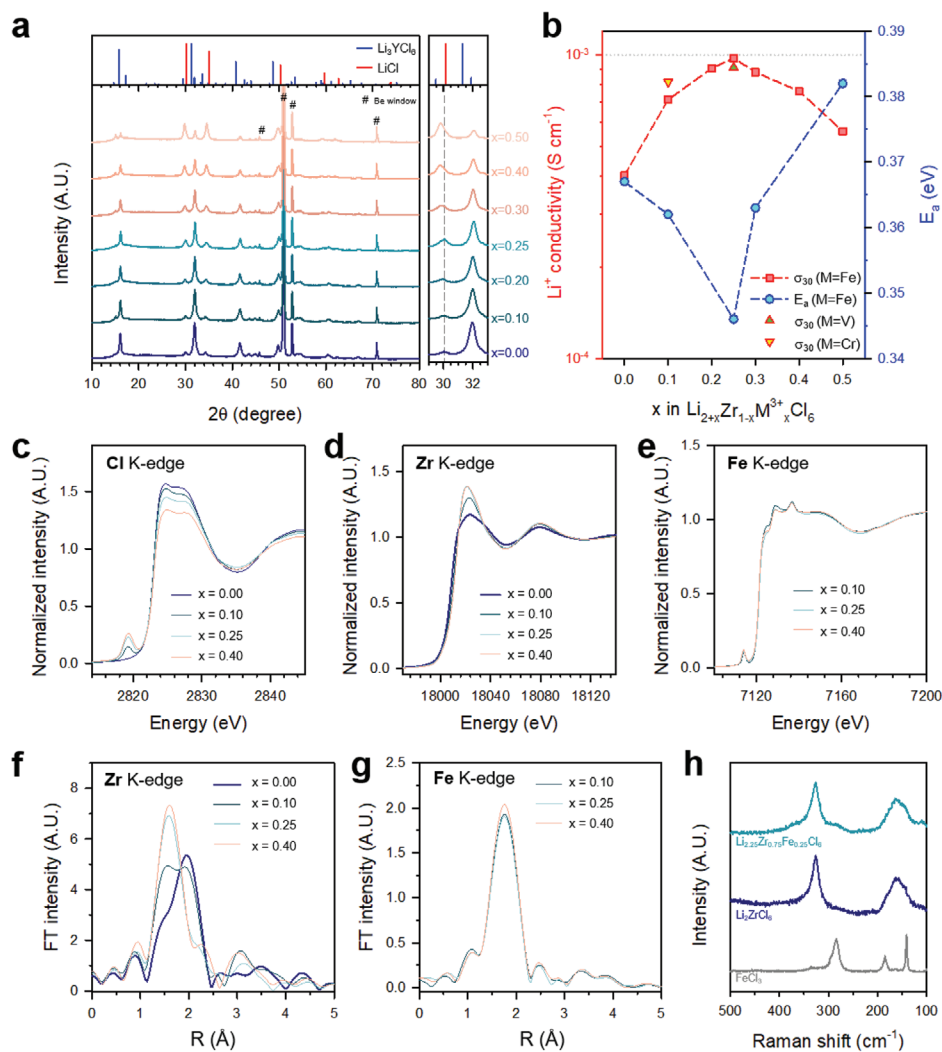**Figure 3.** Characterization of mechanochemically prepared Fe^{3+}-substituted Li_2ZrCl_6 ($Li_{2+x}Zr_{1-x}Fe_xCl_6$). a) XRD patterns for a series of $Li_{2+x}Zr_{1-x}Fe_xCl_6$. Bragg indices for Li_3YCl_6[13] and LiCl (ICSD No. 65485) are shown at the top. b) Li^+ conductivities at 30 °C and activation energy for Fe^{3+}-substituted Li_2ZrCl_6 as a function of x in $Li_{2+x}Zr_{1-x}Fe_xCl_6$. Normalized XANES spectra of Fe^{3+}-substituted Li_2ZrCl_6 for c) Cl K-edge, d) Zr K-edge, and e) Fe K-edge. EXAFS spectra of Fe^{3+}-substituted Li_2ZrCl_6 for f) Zr K-edge and g) Fe K-edge. h) Raman spectra for Fe^{3+}-substituted Li_2ZrCl_6 (BM-$Li_{2.25}Zr_{0.75}Fe_{0.25}Cl_6$), BM-$Li_2ZrCl_6$, and $FeCl_3$.

The local structure of $Li_{2+x}Zr_{1-x}Fe_xCl_6$ was probed using XAS and Raman spectroscopy measurements (Figure 3c–h). Using ligand K-edge XAS, the covalency in metal–ligand bond can be directly measured through the pre-edge intensity originating from the excitation of the ligand p-orbital to the metal antibonding orbital.[58] The Cl K-edge XANES spectra were measured to investigate such bond covalency with Fe^{3+} substitution. As shown in Figure 3c, the pre-edge intensity at 2819 eV in the Cl K-edge XANES significantly increased with Fe^{3+} substitution. Although the pre-edge was not observed in the corresponding Zr K-edge XANES (Figure 3d), the Fe K-edge spectra exhibited clear pre-edge peaks at ≈7114 eV (Figure 3e), which are attributed to the 1s→3d electric dipole forbidden transition by 3d–4p orbital mixing.[59] Therefore, the increased intensity of the pre-edge at the Cl and Fe K-edges with Fe^{3+} substitution is attributed to the increased Fe−Cl bond covalency, while the Zr−Cl bond remains mainly ionic. It should also be noted

that the edge position of Zr and Fe K-edge XAS remained unchanged regardless of the Fe^{3+} substitution, indicating valance states of Zr^{4+} and Fe^{3+} in $Li_{2+x}Zr_{1-x}Fe_xCl_6$. A recent theoretical study using the first-principles molecular dynamics coupled with Wannier analysis revealed that the mixed ionic-covalent characteristics in Li_3InBr_6 and similar halide SEs could enhance Li^+ conductivity by modulating the overall potential energy landscape to facilitate migration.[60] Therefore, well-balanced, mixed ionic-covalent bonding characteristics of the Zr−Cl and Fe−Cl bonds could be responsible for the enhanced ionic conductivity. However, extensive computational and structural studies are necessary to validate this hypothesis.

The Zr K-edge and Fe K-edge EXAFS spectra are shown in Figures 3f and 3g, respectively; corresponding fitted results are provided in Figure S15 and Table S2, Supporting Information. On introducing Fe^{3+} to Li_2ZrCl_6, the average Zr−Cl bond length decreased significantly from 2.46(8) to 2.34(2) Å up to

ADVANCED
SCIENCE NEWS
www.advancedsciencenews.com

ADVANCED
ENERGY
MATERIALS
www.advenergymat.de

$x = 0.25$ and remained roughly the same at $x = 0.40$ (Figure 3f and Table S2, Supporting Information). This result is in good agreement with the solid-solution limit of $x = 0.25$–0.30, as determined via the complementary analyses using XRD and Li$^+$ conductivity measurements (Figure 3a,b). In contrast, the change in the bond length of Fe−Cl was insignificant in the range of $x = 0.10$–0.40 (Figure 3g and Table S2, Supporting Information) from 2.42(7) to 2.44(9) Å. To verify the Fe^{3+} position in BM-Li$_{2+x}$Zr$_{1-x}$Fe$_x$Cl$_6$, the curve fitting analysis for Fe K-edge EXAFS data in the extended R region (1.0–3.8 Å) was performed using a modified trigonal model structure of BM-Li$_2$ZrCl$_6$ (space group $P\bar{3}m1$), where one of the Zr atoms (at Zr1(M1) site) is replaced by Fe. The R and k space fitting results shown in Figure S16, Supporting Information, demonstrated excellent agreement with the measured EXAFS spectra, which confirms the successful substitution of Fe^{3+} in Zr sites. Fitting attempts to replace Zr2(M2) and Zr3(M3) atoms with Fe also resulted in very good agreement factors in EXAFS spectra, which reveal Fe^{3+} ions are randomly substituted into the Zr sites in BM-Li$_2$ZrCl$_6$ structure with mixed M2/M3 site disordering. The shrinkage of the Zr−Cl bond length, as proved by the EXAFS analysis, is due to the increased ionicity in the Zr−Cl bonding caused by the Fe^{3+} substitution. In addition, the shrinkage of Zr−Cl octahedra upon Fe^{3+} substitution could suggest an expansion of the Li$^+$ transport pathways through directly connected face-sharing octahedral sites along the c axis of the hcp structure, which leads to an increased Li$^+$ conductivity.[13] Fe^{3+}-substituted Li$_2$ZrCl$_6$ (Li$_{2.25}$Zr$_{0.75}$Fe$_{0.25}$Cl$_6$) showed a Raman spectrum that was distinctly different from that of the precursor FeCl$_3$ (Figure 3h), confirming a successful mechanochemical reaction. Moreover, the marginal difference in Raman spectra, regardless of Fe^{3+}-substitution, indicates a similar local structure based on octahedrally coordinated polyhedra.[52]

Due to the poor crystalline features of mechanochemically derived Fe^{3+}-substituted Li$_2$ZrCl$_6$, clear-cut characterization of the structure was not possible. Quantitative structural analysis using PDF measurements and/or density functional theory calculations could be effective for further investigations.[16,19,26,34,44,61,62] Nevertheless, several important insights on underlying mechanisms could be deduced. First, the aliovalent substitution increasing the amount of Li$^+$ could raise the concentration of effective charge carriers, which universally occurs in solid-state ionics.[35,44,55,56,63] In the classical example of the solid solution between Li$_4$SiO$_4$ and Li$_{2.5}$Al$_{0.5}$SiO$_4$, where there are fully occupied and empty Li$^+$ sites, respectively, the highest Li$^+$ conductivity is achieved at an optimal concentration of Li$^+$ and vacancies.[64] Moreover, for a popular sulfide Na$^+$ superionic conductor, Na$_3$PS$_4$, it was elucidated that the formation of Na$^+$ vacancies by aliovalent substitution (e.g., Na$_{3-2x}$Ca$_x$PS$_4$ and Na$_{3-x}$PS$_{1-x}$Cl$_x$) was critical for enhancing the conductivity of Na$^+$.[44,65] Second, the aliovalent substitution of Zr^{4+} with trivalent metal ions, Fe^{3+}, could relieve Coulombic repulsion between Li$^+$ and other metal cations, and thus lower the activation barrier for Li$^+$ transport.[34] Third, the EXAFS results showed an overall reduced size of central atom polyhedra, which may be translated into enlarged Li$^+$ channels, rendering more facile Li$^+$ transport.[26,43]

The new halide SEs of BM-Li$_2$ZrCl$_6$ and BM-Li$_{2.25}$Zr$_{0.75}$Fe$_{0.25}$Cl$_6$ showed excellent stability upon exposure to dry air for 6 h (Figure S17 and Table S3, Supporting Information). Electrochemical stability window of BM-Li$_2$ZrCl$_6$ was also assessed via cyclic voltammetry measurements (Figure S18, Supporting Information). BM-Li$_2$ZrCl$_6$ showed excellent oxidation stability at high voltage region (2.0–5.0 V [Li/Li$^+$]) but poor reduction stability at low voltage region (0.0–3.0 V [Li/Li$^+$]), which is common for halide SEs.[13,33,36,39] Interfacial engineering that might enable halide SEs working with Li metal anode would be an interesting future research.[8,66–70]

The mechanochemically prepared halide SEs, Li$_{2+x}$Zr$_{1-x}$Fe$_x$Cl$_6$, were applied for cathodes using LiCoO$_2$ without any protective coating layers in all-solid-state cells tested at 30 °C (**Figure 4**a–f). Figure 4a shows first-cycle charge–discharge voltage profiles at 0.1C (16 mA g^{-1}) for the LiCoO$_2$ electrodes using BM-Li$_2$ZrCl$_6$, BM-Li$_{2.25}$Zr$_{0.75}$Fe$_{0.25}$Cl$_6$, and Li$_6$PS$_5$Cl. LiCoO$_2$ employing sulfide SE Li$_6$PS$_5$Cl showed a distinctly different feature at the beginning of first charge compared with that which employed halide SEs: the sloping voltage profile starting at ≈3.2 V (vs Li/Li$^+$) (indicated by an arrow) confirmed the poor electrochemical oxidation stability of sulfide SEs.[18] Moreover, substantial polarization was observed in voltage profiles when Li$_6$PS$_5$Cl was used, and a consequently low discharge capacity of 127 mA h g^{-1} and poor initial Coulombic efficiency of 86.2% were obtained. In contrast, the LiCoO$_2$ electrodes employing Li$_2$ZrCl$_6$ and Li$_{2.25}$Zr$_{0.75}$Fe$_{0.25}$Cl$_6$ exhibited high first discharge capacities of 156 and 162 mA h g^{-1} with high initial Columbic efficiencies of 91.4% and 90.5%, respectively. Moreover, the rate capabilities of the LiCoO$_2$ electrodes using Li$_2$ZrCl$_6$ and Li$_{2.25}$Zr$_{0.75}$Fe$_{0.25}$Cl$_6$ were significantly superior to those using Li$_6$PS$_5$Cl (Figure 4b) despite the higher Li$^+$ conductivity of Li$_6$PS$_5$Cl (4.8 mS cm^{-1}) than those of Li$_2$ZrCl$_6$ (0.40 mS cm^{-1}) and Li$_{2.25}$Zr$_{0.75}$Fe$_{0.25}$Cl$_6$ (0.98 mS cm^{-1}). This result emphasizes that not only Li$^+$ conductivity but also interfacial resistance plays a decisive role in the overall kinetics of all-solid-state cells.[13,71] In addition, the better rate capability obtained for Li$_{2.25}$Zr$_{0.75}$Fe$_{0.25}$Cl$_6$ than that for Li$_2$ZrCl$_6$ highlights the high Li$^+$ conductivity of ≈1 mS cm^{-1} for Li$_{2.25}$Zr$_{0.75}$Fe$_{0.25}$Cl$_6$. Furthermore, excellent cycling stability of the LiCoO$_2$ electrodes employing halide SE Li$_2$ZrCl$_6$ was confirmed (Figure 4c). Capacity retention after 100 cycles while using Li$_2$ZrCl$_6$ was 90.5%, which is notably different from that while using Li$_6$PS$_5$Cl (59.9%). Interfacial stabilities between LiCoO$_2$ and SEs while using Li$_6$PS$_5$Cl or Li$_2$ZrCl$_6$ were assessed by electrochemical impedance spectroscopy (EIS) measurements, and corresponding Nyquist plots at the second and tenth cycles are shown in Figure 4d. The amplitude of semicircles in the Nyquist plots corresponds to the LiCoO$_2$–SE interfacial resistance.[18,23,24,27] The fitted value at the second cycle while using Li$_2$ZrCl$_6$ was only ≈27 Ω, while that using Li$_6$PS$_5$Cl was as high as ≈650 Ω, confirming the outstanding interfacial stability of Li$_2$ZrCl$_6$. The underlying interfacial (electro)chemistry was probed by ex situ XPS measurements of the LiCoO$_2$ electrodes employing Li$_2$ZrCl$_6$ for pristine electrodes and after 100 cycles (Figure 4e,f). Marginal changes were observed after 100 cycles for the spectra of Zr 3d and Cl 2p, corroborating the intactness of Li$_2$ZrCl$_6$. In short, the electrochemical and ex situ XPS measurements unambiguously confirm the excellent stability of Li$_2$ZrCl$_6$ when operated in contact with bare LiCoO$_2$.
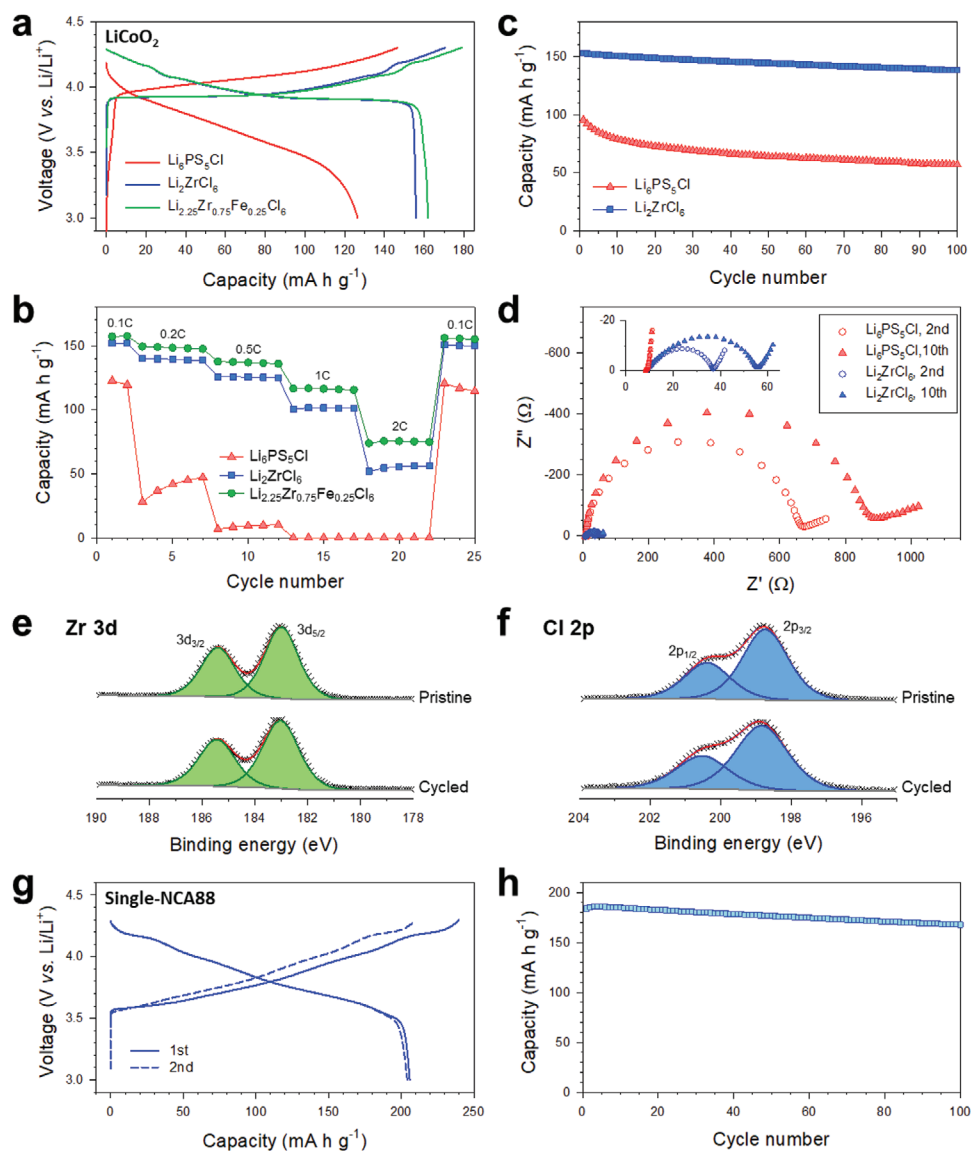
Figure 4. Electrochemical characterization of $LiMO_2$/Li–In all-solid-state cells employing BM-$Li_{2+x}Zr_{1-x}Fe_xCl_6$ at 30 °C. a) First-cycle charge–discharge voltage profiles at 0.1C for $LiCoO_2$ electrodes using Li_6PS_5Cl, Li_2ZrCl_6, and $Li_{2.25}Fe_{0.25}Zr_{0.75}Cl_6$, and b) corresponding rate capabilities. c) Cycling performances at 0.5C and d) corresponding Nyquist plots for $LiCoO_2$ electrodes using Li_6PS_5Cl and Li_2ZrCl_6. The cells were charged without and with a constant-voltage mode (the limiting current: 0.1C) for (b) and (c), respectively. Ex situ XPS signals of e) Zr 3d and f) Cl 2p for $LiCoO_2$ electrodes using Li_2ZrCl_6 for pristine powders and electrodes after 100 cycles. g) First two-cycle charge–discharge voltage profiles at 0.1C for single-NCA88 (single-crystalline $Li_{0.88}Co_{0.11}Al_{0.01}O_2$) electrodes employing Li_2ZrCl_6 and h) corresponding cycling performance at 0.5C.

The $LiCoO_2$ electrodes using BM-$Li_{2.25}Zr_{0.75}Fe_{0.25}Cl_6$ with the highest conductivity also outperformed those using the sulfide SE Li_6PS_5Cl significantly but at the expense of degraded cycling performance, as compared to those using BM-Li_2ZrCl_6 (Figure S19, Supporting Information). The substituted Fe^{3+} may undergo an oxidation to Fe^{4+} upon charge, which would be detrimental to the stability of SE and thus facile $LiCoO_2$–SE interfacial Li^+ transports.[16,37,45,71] Importantly, the similar cycling performance, as compared to the unsubstituted BM-Li_2ZrCl_6, with the better rate capability, was achieved by lowering the amount of Fe^{3+} doping down to $x = 0.10$.

Finally, the applicability of Li_2ZrCl_6 to newly emerging single-crystalline layered oxide cathodes, specifically uncoated

single-NCA88, was assessed (Figure 4g,h). First two-cycle voltage profiles at 0.1C for the single-NCA88 electrodes using Li_2ZrCl_6 are displayed in Figure 4g, showing a high discharge capacity of 206 mA h g^{-1} and high initial Coulombic efficiency of 85.8%. The single-NCA88 combined with Li_2ZrCl_6 also showed a high capacity retention of 91.3% after 100 cycles. In our previous study, we demonstrated that secondary particles of commercial-grade $LiNi_{0.80}Co_{0.10}Al_{0.10}O_2$ consisting of randomly oriented grains were prone to severe disintegration in all-solid-state cells even at the initial cycles, leading to the poor initial Coulombic efficiency and fast capacity fading upon repeated cycling.[72] The good electrochemical performance of the single-NCA88 electrodes employing Li_2ZrCl_6 could thus be

attributed to the mechanical integrity of the single-crystalline feature of NCA88, as well as to the negligible side reaction of Li_2ZrCl_6.[73–76]

In summary, new halide superionic conductors, hcp Li_2ZrCl_6 and Fe^{3+}-substituted Li_2ZrCl_6, were synthesized by a mechanochemical method using inexpensive and earth-abundant elements. The heat treatment of Li_2ZrCl_6 led to a ccp-based monoclinic structure with low Li^+ conductivity of 5.7×10^{-6} S cm^{-1} at 30 °C, and the ball-milling method produced an hcp structure with a high Li^+ conductivity of 0.40 mS cm^{-1}, which is abnormal in the family of halide SEs. Furthermore, it was demonstrated that the aliovalent substitution of Li_2ZrCl_6 with Fe^{3+} significantly enhanced Li^+ conductivity up to ≈1 mS cm^{-1} ($Li_{2.25}Zr_{0.75}Fe_{0.25}Cl_6$). The aliovalent substitution with alternative trivalent metals including Cr^{3+} and V^{3+} was also effective in improving Li^+ conductivity. The combined structural analysis using XRD, PDF, XAS, and Raman spectroscopy revealed the evolution of the solid-solution phase in the hcp structure Fe^{3+}-substituted Li_2ZrCl_6. Specifically, the shrinkage of $ZrCl_6^{2-}$ octahedra and the increased bond covalency upon Fe^{3+} substitution was probed, which might indicate enlarged Li^+ channels and regulated energy landscape for favorable Li^+ migration, respectively. Moreover, the metal site disordering in $BM\text{-}Li_{2+x}Zr_{1-x}Fe_xCl_6$, which could contribute to the enhanced Li^+ migration, was confirmed. Finally, the excellent interfacial stability of the new $Li_{2+x}Zr_{1-x}Fe_xCl_6$ combined with $LiCoO_2$ or single-NCA88 electrodes was demonstrated via the electrochemical and ex situ XPS measurements. Our results demonstrate a breakthrough in practical all-solid-state technologies and provide an intriguing viewpoint for designing new halide superionic conductors.

Experimental Section

Preparation of Materials: For the preparation of $Li_{2+x}Zr_{1-x}Fe_xCl_6$, a stoichiometric mixture of LiCl (99.99%, Sigma Aldrich), $ZrCl_4$ (99.99%, Sigma Aldrich), and $FeCl_3$ (99.9%, Sigma Aldrich) was BM at 600 rpm for 10 h in a ZrO_2 vial with ZrO_2 balls using Pulverisette 7PL (Fritsch GmbH). For further heat treatment, the BM powders were annealed at 260 °C for 12 h in a fused silica ampoule sealed under vacuum. For the preparation of Li_6PS_5Cl, a stoichiometric mixture of Li_2S (99.9%, Alfa Aesar), P_2S_5 (99%, Sigma Aldrich), and LiCl (99.99%, Sigma Aldrich) was BM at 600 rpm for 10 h in a ZrO_2 vial with ZrO_2 balls, followed by annealing at 550 °C for 5 h under an Ar atmosphere. Single-NCA88 powders were provided by EcoPro BM.

Materials Characterization: For the dry-air stability test, 200 mg of SE powder samples was exposed to continuous flow of dry air (a mixture of N_2 and O_2 with 79/21 vol. ratio). Inductively coupled plasma optical emission spectroscopy measurements were employed using OPTIMA 8300 (PerkinElmer Inc.), and confirmed the Zr to Fe atomic ratios for the nominal compositions $Li_{2+x}Zr_{1-x}Fe_xCl_6$. Powder XRD patterns were collected using a Rigaku MiniFlex600 diffractometer with Cu K_α radiation ($\lambda = 1.5406$ Å). XRD cells containing hermetically sealed SE samples with a beryllium window were mounted on an XRD diffractometer and measured at 40 kV and 15 mA. X-ray total-scattering data were collected at beamline 28-ID-1 at the National Synchrotron Light Source II Brookhaven National Laboratory with an X-ray energy of 74.5 keV ($\lambda = 0.1665$ Å). Prepared samples were loaded in polyimide (Kapton) tubes and hermetically sealed with epoxy resin. The 2D image was integrated and converted to 1D diffraction pattern with Ni calibration standard using Dioptas software.[77] The PDF was obtained

from sine Fourier transforming the $F(Q)$ with a Q range up to 24.5 Å using xPDFsuite software package.[78] The Fe and Zr K-edge XAS was conducted at the 7D and 10C beamline of Pohang Accelerator Laboratory using a Si (111) double-crystal monochromator in transmission and fluorescence mode. The energy calibration was carried out with the reference spectra of Fe and Zr metal foils. The Cl K-edge XANES spectra were measured in fluorescence yield mode at the 16A1 of Taiwan Light Source. XANES and EXAFS data were processed using the Demeter software package. SEM images were obtained using AURIGA (Zeiss). To avoid air exposure of the samples, an air-tight transfer box, DME 2830 (SEMILAB), was used. Raman spectra were collected with an Ar-ion laser beam at an exciting radiation wavelength of 514.5 nm using a LabRam Aramis (Horiba Jobin Yvon). The ex situ XPS measurements were carried out with a monochromatic Al K_α source (1486.6 eV) at 12 kV and 6 mA using K-Alpha+ (Thermo Fisher Scientific). The samples were mounted on a sample holder in an Ar-filled glove box and transferred into the XPS equipment without exposure to air.

Electrochemical Characterization: Li^+ conductivities were measured by the AC impedance method using Li^+-blocking Ti/SE/Ti symmetric cells. The cold-pressed pellets were prepared at 370 MPa. The EIS data were recorded at an amplitude of 100 mV and a frequency range from 10 mHz to 7 MHz using a VMP3 (Bio-Logic). For the all-solid-state half-cells, a Li–In counter and reference electrodes were used. After the Li–In powders with a nominal composition of $Li_{0.5}In$ were prepared by ball-milling of In (Aldrich, 99%) and Li (FMC Lithium Corp.), they were then mixed with Li_6PS_5Cl powders in a weight ratio of 8:2. Li_6PS_5Cl powders (150 mg) were pelletized under 100 MPa to form SE layers. Composite working electrodes were prepared from a mixture of $LiCoO_2$ or single-NCA88, $Li_{2+x}Zr_{1-x}Fe_xCl_6$, and super C65 powders at a weight ratio of 70:30:3. Finally, the $LiCoO_2$ or single-NCA88 electrodes and the Li–In electrodes were attached on either side of the SE layers, and the whole assembly was pressed at 370 MPa. The all-solid-state cells were tested under an external pressure of ≈70 MPa. The EIS measurements for the cells were performed from 1.5 MHz to 5 mHz at an amplitude of 10 mV after discharging the cells to 3.93 V (vs Li/Li^+) for Li_2ZrCl_6 and 3.67 V (vs Li/Li^+) for LPSCl at 0.1C at the second and tenth cycles.

Supporting Information

Supporting Information is available from the Wiley Online Library or from the author.

Conflict of Interest

The authors declare no conflict of interest.

[1] J. Janek, W. G. Zeier, *Nat. Energy* **2016**, *1*, 16141.

[2] K. Kerman, A. Luntz, V. Viswanathan, Y.-M. Chiang, Z. Chen, *J. Electrochem. Soc.* **2017**, *164*, A1731.

[3] K. H. Park, Q. Bai, D. H. Kim, D. Y. Oh, Y. Zhu, Y. Mo, Y. S. Jung, *Adv. Energy Mater.* **2018**, *8*, 1800035.

[4] Z. Zhang, Y. Shao, B. Lotsch, Y.-S. Hu, H. Li, J. Janek, L. F. Nazar, C.-W. Nan, J. Maier, M. Armand, L. Chen, *Energy Environ. Sci.* **2018**, *11*, 1945.

[5] Q. Zhang, D. Cao, Y. Ma, A. Natan, P. Aurora, H. Zhu, *Adv. Mater.* **2019**, *31*, 1901131.

[6] R. Chen, Q. Li, X. Yu, L. Chen, H. Li, *Chem. Rev.* **2020**, *120*, 6820.

[7] Y. Kato, S. Hori, T. Saito, K. Suzuki, M. Hirayama, A. Mitsui, M. Yonemura, H. Iba, R. Kanno, *Nat. Energy* **2016**, *1*, 16030.

[8] X. Han, Y. Gong, K. K. Fu, X. He, G. T. Hitz, J. Dai, A. Pearse, B. Liu, H. Wang, G. Rubloff, Y. Mo, V. Thangadurai, E. D. Wachsman, L. Hu, *Nat. Mater.* **2017**, *16*, 572.

[9] H. J. Deiseroth, S. T. Kong, H. Eckert, J. Vannahme, C. Reiner, T. Zaiss, M. Schlosser, *Angew. Chem., Int. Ed.* **2008**, *47*, 755.

[10] S. Stramare, V. Thangadurai, W. Weppner, *Chem. Mater.* **2003**, *15*, 3974.

[11] L. Duchêne, A. Remhof, H. Hagemann, C. Battaglia, *Energy Storage Mater.* **2020**, *25*, 782.

[12] S. Kim, H. Oguchi, N. Toyama, T. Sato, S. Takagi, T. Otomo, D. Arunkumar, N. Kuwata, J. Kawamura, S. I. Orimo, *Nat. Commun.* **2019**, *10*, 1081.

[13] T. Asano, A. Sakai, S. Ouchi, M. Sakaida, A. Miyazaki, S. Hasegawa, *Adv. Mater.* **2018**, *30*, 1803075.

[14] A. Manthiram, X. Yu, S. Wang, *Nat. Rev. Mater.* **2017**, *2*, 16103.

[15] K. H. Kim, Y. Iriyama, K. Yamamoto, S. Kumazaki, T. Asaka, K. Tanabe, C. A. J. Fisher, T. Hirayama, R. Murugan, Z. Ogumi, *J. Power Sources* **2011**, *196*, 764.

[16] Y. Zhu, X. He, Y. Mo, *ACS Appl. Mater. Interfaces* **2015**, *7*, 23685.

[17] J. van den Broek, S. Afyon, J. L. M. Rupp, *Adv. Energy Mater.* **2016**, *6*, 1600736.

[18] A. Sakuda, A. Hayashi, M. Tatsumisago, *Chem. Mater.* **2010**, *22*, 949.

[19] Y. H. Xiao, Y. Wang, S. H. Bo, J. C. Kim, L. J. Miara, G. Ceder, *Nat. Rev. Mater.* **2020**, *5*, 105.

[20] Y. Li, X. Wang, H. Zhou, X. Xing, A. Banerjee, J. Holoubek, H. Liu, Y. S. Meng, P. Liu, *ACS Energy Lett.* **2020**, *3*, 955.

[21] H. Muramatsu, A. Hayashi, T. Ohtomo, S. Hama, M. Tatsumisago, *Solid State Ionics* **2011**, *182*, 116.

[22] Y. Zhu, Y. Mo, *Angew. Chem. Int. Ed.* **2020**, *59*, 17472.

[23] K. H. Park, D. Y. Oh, Y. E. Choi, Y. J. Nam, L. Han, J. Y. Kim, H. Xin, F. Lin, S. M. Oh, Y. S. Jung, *Adv. Mater.* **2016**, *28*, 1874.

[24] A. Banerjee, K. H. Park, J. W. Heo, Y. J. Nam, C. K. Moon, S. M. Oh, S. T. Hong, Y. S. Jung, *Angew. Chem., Int. Ed.* **2016**, *55*, 9634.

[25] Y. E. Choi, K. H. Park, D. H. Kim, D. Y. Oh, H. R. Kwak, Y. G. Lee, Y. S. Jung, *ChemSusChem* **2017**, *10*, 2605.

[26] H. Kwak, D. Han, K.-W. Nam, H. Kim, Y. S. Jung, *J. Power Sources* **2020**, *446*, 227338.

[27] S. H. Jung, K. Oh, Y. J. Nam, D. Y. Oh, P. Brüner, K. Kang, Y. S. Jung, *Chem. Mater.* **2018**, *30*, 8190.

[28] T. Hakari, M. Deguchi, K. Mitsuhara, T. Ohta, K. Saito, Y. Orikasa, Y. Uchimoto, Y. Kowada, A. Hayashi, M. Tatsumisago, *Chem. Mater.* **2017**, *29*, 4768.

[29] W. Zhang, T. Leichtweiss, S. P. Culver, R. Koerver, D. Das, D. A. Weber, W. G. Zeier, J. Janek, *ACS Appl. Mater. Interfaces* **2017**, *9*, 35888.

[30] A. Banerjee, X. Wang, C. Fang, E. A. Wu, Y. S. Meng, *Chem. Rev.* **2020**, *120*, 6878.

[31] T. K. Schwietert, V. A. Arszelewska, C. Wang, C. Yu, A. Vasileiadis, N. J. J. de Klerk, J. Hageman, T. Hupfer, I. Kerkamm, Y. Xu, E. van der Maas, E. M. Kelder, S. Ganapathy, M. Wagemaker, *Nat. Mater.* **2020**, *19*, 428.

[32] X. Li, J. Liang, X. Yang, K. R. Adair, C. Wang, F. Zhao, X. Sun, *Energy Environ. Sci.* **2018**, *11*, 719.

[33] X. Li, J. Liang, J. Luo, M. Norouzi Banis, C. Wang, W. Li, S. Deng, C. Yu, F. Zhao, Y. Hu, T.-K. Sham, L. Zhang, S. Zhao, S. Lu, H. Huang, R. Li, K. R. Adair, X. Sun, *Energy Environ. Sci.* **2019**, *12*, 2665.

[34] R. Schlem, S. Muy, N. Prinz, A. Banik, Y. Shao-Horn, M. Zobel, W. G. Zeier, *Adv. Energy Mater.* **2020**, *10*, 1903719.

[35] K.-H. Park, K. Kaup, A. Assoud, Q. Zhang, X. Wu, L. F. Nazar, *ACS Energy Lett.* **2020**, *5*, 533.

[36] J. Liang, X. Li, S. Wang, K. R. Adair, W. Li, Y. Zhao, C. Wang, Y. Hu, L. Zhang, S. Zhao, S. Lu, H. Huang, R. Li, Y. Mo, X. Sun, *J. Am. Chem. Soc.* **2020**, *142*, 7012.

[37] S. Wang, Q. Bai, A. M. Nolan, Y. Liu, S. Gong, Q. Sun, Y. Mo, *Angew. Chem., Int. Ed.* **2019**, *58*, 8039.

[38] H. J. Steiner, H. D. Lutz, *Z. Anorg. Allg. Chem.* **1992**, *613*, 26.

[39] L. Zhou, C. Y. Kwok, A. Shyamsunder, Q. Zhang, X. Wu, L. F. Nazar, *Energy Environ. Sci.* **2020**, *13*, 2056.

[40] W. M. Haynes, *CRC Handbook of Chemistry and Physics*, 97th ed., CRC Press, Boca Raton, FL **2016**.

[41] A. Bohnsack, G. Balzer, H.-U. Gdel, M. S. Wickleder, G. Meyer, *Z. Anorg. Allg. Chem.* **1997**, *623*, 1352.

[42] R. Schlem, T. Bernges, C. Li, M. A. Kraft, N. Minafra, W. G. Zeier, *ACS Appl. Energy Mater.* **2020**, *3*, 3684.

[43] Z. Yu, S. L. Shang, J. H. Seo, D. Wang, X. Luo, Q. Huang, S. Chen, J. Lu, X. Li, Z. K. Liu, D. Wang, *Adv. Mater.* **2017**, *29*, 1605561.

[44] C. K. Moon, H.-J. Lee, K. H. Park, H. Kwak, J. W. Heo, K. Choi, H. Yang, M.-S. Kim, S.-T. Hong, J. H. Lee, Y. S. Jung, *ACS Energy Lett.* **2018**, *3*, 2504.

[45] S. P. Ong, Y. Mo, W. D. Richards, L. Miara, H. S. Lee, G. Ceder, *Energy Environ. Sci.* **2013**, *6*, 148.

[46] S. Muy, J. Voss, R. Schlem, R. Koerver, S. J. Sedlmaier, F. Maglia, P. Lamp, W. G. Zeier, Y. Shao-Horn, *iScience* **2019**, *16*, 270.

[47] Y. Okamoto, H. Motohashi, *Zeitschrift für Naturforschung A* **2002**, *57*, 277.

[48] Y. Okamoto, T. Yaita, H. Shiwaku, S. Suzuki, *Zeitschrift für Naturforschung A* **2008**, *63*, 735.

[49] B. Krebs, *Angew. Chem., Int. Ed.* **1969**, *8*, 146.

[50] D. H. Kim, Y.-H. Lee, Y. B. Song, H. Kwak, S.-Y. Lee, Y. S. Jung, *ACS Energy Lett.* **2020**, *5*, 718.

[51] Y. B. Song, D. H. Kim, H. Kwak, D. Han, S. Kang, J. H. Lee, S. M. Bak, K. W. Nam, H. W. Lee, Y. S. Jung, *Nano Lett.* **2020**, *20*, 4337.

[52] G. M. Photiadis, G. N. Papatheodorou, *J. Chem. Soc., Dalton Trans.* **1998**, 981, https://pubs.rsc.org/en/content/articlehtml/1998/dt/a707126d.

[53] K. Biswas, M.-H. Du, *Phys. Rev. B* **2012**, *86*, 014102.

[54] G. Papatheodorou, *J. Chem. Phys.* **1977**, *66*, 2893.

[55] M. A. Kraft, S. Ohno, T. Zinkevich, R. Koerver, S. P. Culver, T. Fuchs, A. Senyshyn, S. Indris, B. J. Morgan, W. G. Zeier, *J. Am. Chem. Soc.* **2018**, *140*, 16330.

[56] L. Zhou, A. Assoud, Q. Zhang, X. Wu, L. F. Nazar, *J. Am. Chem. Soc.* **2019**, *141*, 19002.

[57] A. Hayashi, N. Masuzawa, S. Yubuchi, F. Tsuji, C. Hotehama, A. Sakuda, M. Tatsumisago, *Nat. Commun.* **2019**, *10*, 5266.

[58] S. A. Kozimor, P. Yang, E. R. Batista, K. S. Boland, C. J. Burns, D. L. Clark, S. D. Conradson, R. L. Martin, M. P. Wilkerson, L. E. Wolfsberg, *J. Am. Chem. Soc.* **2009**, *131*, 12125.

[59] T. E. Westre, P. Kennepohl, J. G. DeWitt, B. Hedman, K. O. Hodgson, E. I. Solomon, *J. Am. Chem. Soc.* **1997**, *119*, 6297.

[60] N. Adelstein, B. C. Wood, *Chem. Mater.* **2016**, *28*, 7218.

[61] Y. Qie, S. Wang, S. Fu, H. Xie, Q. Sun, P. Jena, *J. Phys. Chem. Lett.* **2020**, *11*, 3376.

[62] T. Famprikis, P. Canepa, J. A. Dawson, M. S. Islam, C. Masquelier, *Nat. Mater.* **2019**, *18*, 1278.

[63] P. Wang, H. Liu, S. Patel, X. Feng, P.-H. Chien, Y. Wang, Y.-Y. Hu, *Chem. Mater.* **2020**, *32*, 3833.

[64] A. R. West, *Solid State Chemistry and its Applications*, John Wiley & Sons, New York **2014**.

[65] I.-H. Chu, C. S. Kompella, H. Nguyen, Z. Zhu, S. Hy, Z. Deng, Y. S. Meng, S. P. Ong, *Sci. Rep.* **2016**, *6*, 33733.

[66] Y. Huang, B. Chen, J. Duan, F. Yang, T. Wang, Z. Wang, W. Yang, C. Hu, W. Luo, Y. Huang, *Angew. Chem., Int. Ed.* **2020**, *59*, 3699.

[67] K. Shi, Z. Wan, L. Yang, Y. Zhang, Y. Huang, S. Su, H. Xia, K. Jiang, L. Shen, Y. Hu, S. Zhang, J. Yu, F. Ren, Y.-B. He, F. Kang, *Angew. Chem., Int. Ed.* **2020**, *59*, 11784.

[68] X. Hao, Q. Zhao, S. Su, S. Zhang, J. Ma, L. Shen, Q. Yu, L. Zhao, Y. Liu, F. Kang, Y.-B. He, *Adv. Energy Mater.* **2019**, *9*, 1901604.

[69] Z. Wan, D. Lei, W. Yang, C. Liu, K. Shi, X. Hao, L. Shen, W. Lv, B. Li, Q.-H. Yang, F. Kang, Y.-B. He, *Adv. Funct. Mater.* **2019**, *29*, 1805301.

[70] Y.-G. Lee, S. Fujiki, C. Jung, N. Suzuki, N. Yashiro, R. Omoda, D.-S. Ko, T. Shiratsuchi, T. Sugimoto, S. Ryu, J. H. Ku, T. Watanabe, Y. Park, Y. Aihara, D. Im, I. T. Han, *Nat. Energy* **2020**, *5*, 299.

[71] E. McCalla, M. T. Sougrati, G. Rousse, E. J. Berg, A. Abakumov, N. Recham, K. Ramesha, M. Sathiya, R. Dominko, G. Van Tendeloo, P. Novak, J.-M. Tarascon, *J. Am. Chem. Soc.* **2015**, *137*, 4804.

[72] S. H. Jung, U.-H. Kim, J.-H. Kim, S. Jun, C. S. Yoon, Y. S. Jung, Y.-K. Sun, *Adv. Energy Mater.* **2020**, *10*, 1903360.

[73] H. Li, J. Li, N. Zaker, N. Zhang, G. A. Botton, J. R. Dahn, *J. Electrochem. Soc.* **2019**, *166*, A1956.

[74] X. Fan, G. Hu, B. Zhang, X. Ou, J. Zhang, W. Zhao, H. Jia, L. Zou, P. Li, Y. Yang, *Nano Energy* **2020**, *70*, 104450.

[75] J. Kim, H. Lee, H. Cha, M. Yoon, M. Park, J. Cho, *Adv. Energy Mater.* **2018**, *8*, 1702028.

[76] F. A. Susai, H. Sclar, Y. Shilina, T. R. Penki, R. Raman, S. Maddukuri, S. Maiti, I. C. Halalay, S. Luski, B. Markovsky, D. Aurbach, *Adv. Mater.* **2018**, *30*, 1801348.

[77] C. Prescher, V. B. Prakapenka, *High Pressure Res.* **2015**, *35*, 223.

[78] X. Yang, P. Juhas, C. L. Farrowa, S. J. L. Billinge, *arXiv:1402.3163*, **2014**.

2003190 (10 of 10)